



**HAL**  
open science

## Two-layer elastic models for single-yeast compressibility with flat microlevers.

Léo Delmarre, Etienne Harté, Anne Devin, Pierre Argoul, Françoise Argoul

### ► To cite this version:

Léo Delmarre, Etienne Harté, Anne Devin, Pierre Argoul, Françoise Argoul. Two-layer elastic models for single-yeast compressibility with flat microlevers.. 2023. hal-04260141

**HAL Id: hal-04260141**

**<https://hal.science/hal-04260141>**

Preprint submitted on 26 Oct 2023

**HAL** is a multi-disciplinary open access archive for the deposit and dissemination of scientific research documents, whether they are published or not. The documents may come from teaching and research institutions in France or abroad, or from public or private research centers.

L'archive ouverte pluridisciplinaire **HAL**, est destinée au dépôt et à la diffusion de documents scientifiques de niveau recherche, publiés ou non, émanant des établissements d'enseignement et de recherche français ou étrangers, des laboratoires publics ou privés.

# Two-layer elastic models for single-yeast compressibility with flat microlevers.<sup>†</sup>

L. Delmarre,<sup>a</sup> E. Harté,<sup>a</sup> A. Devin,<sup>b</sup> P. Argoul<sup>c,d</sup> and F. Argoul<sup>\*a</sup>

Unicellular organisms such as yeast can survive in very different environments thanks to a polysaccharide wall that reinforces their extracellular membrane. This wall is not a static structure, as it is expected to be dynamically remodeled according to growth stage, division cycle, environmental osmotic pressure and ageing. It is therefore of great interest to study the mechanics of these organisms, but they are more difficult to study than other mammalian cells, in particular because of their small size (radius of a few microns) and their lack of an adhesion machinery. Using flat cantilevers, we perform compression experiments on single yeast cells (*S. cerevisiae*) on poly-L-lysine-coated grooved glass plates, in the limit of small deformation using an atomic force microscope (AFM). Thanks to a careful decomposition of force-displacement curves, we extract local scaling exponents that highlight the non-stationary characteristic of the yeast behavior upon compression. Our multi-scale nonlinear analysis of the AFM force-displacement curves provides evidence for non-stationary scaling laws. We propose to model these phenomena based on a two-component elastic system, where each layer follows a different scaling law.

## 1 Introduction

Among natural kingdoms, plants, fungi and unicellular microorganisms (yeasts, bacteria, algae ...) differ from multicellular animals by their intracellular structure and a rigid wall that reinforces the extracellular membrane and can sustain quite high turgor pressure (from 0.5 MPa in exponential growth phase to 1.5 MPa in the stationary phase for yeast)<sup>1</sup>. These cells regulate their volume, depending on the drop of pressure between the intracellular ( $\Pi_i$ ) and the extracellular media ( $\Pi_e$ ), the difference  $\Delta P = \Pi_i - \Pi_e$  is defined as the turgor pressure. Even if yeast cells have rather simple geometries, their mechanical behavior integrates different mechanical forces; compressive (or tensile) and shear forces from their environment with turgor pressure derived forces. *Saccharomyces cerevisiae*, also called the budding yeast, that is investigated here, has often been approximated by spherical shells. Actually its shape is more elliptical than spherical, leading to a preferential position (polarization) of its bud which is driven by turgor pressure during mitosis<sup>2</sup>. Thanks to its  $\beta$ -glucan and titin cross-linked chains<sup>3</sup>, the yeast cell wall (YCW) primary role is to compensate the tensional stress generated by turgor pressure. Assuming that the YCW thickness is negligible versus the cell radius, for a typical cell radius  $R$  of 2.5  $\mu\text{m}$ , the tension  $T$  created by a turgor pressure of  $\Delta P = 1\text{MPa}$  would be<sup>4</sup>  $T = PR/2 = 1.25\text{N/m}$ . The YCW tension appears therefore as a compromise for both cell division and survival. Compression experiments that exceed this wall tension may lead to cascades of local ruptures or unbinding of the wall glucan chains and finally a global disruption<sup>5</sup>. Cascades of local fracture events observed in living cell fiber networks were described with one-dimensional catastrophe models following lognormal statistics<sup>6–8</sup>.

Since the early nineties, the atomic force microscope (AFM)

emerged as a powerful tool because of its ability to probe biomaterials from nanometre scales (biomolecules) up to several tens of micron scales (subcellular organelles, cells, multicellular organisms) with forces in the range of tens to hundreds of nanoNewtons, under near physiological conditions<sup>9</sup>. The enthusiasm of the scientific community for this technique never faded away, and it is now a gold standard for cellular imaging and viscoelasticity measurements at molecular and cellular scales<sup>10,11</sup>. Whereas AFM was immediately and predominantly used as a surface imaging technique for micro-organisms (see chapter 3 of<sup>10</sup> and<sup>12</sup>), different imaging protocols were tested with liquid or with dried samples, facilitated by the robustness of these microorganisms thanks to their wall. Measuring and interpreting the short and long range forces involved in AFM indentation on microorganisms such as bacteria was not straightforward<sup>13</sup>, as it required taking into account both surface interaction forces and submolecular mechanical responses (viscoelasticity, hyperelasticity, damage) of the cells to external stresses or strains. The discrepancy between sharp indentation experiments (small deformations) and micromanipulations (large deformations) remained a source of confusion. AFM indentation on microorganisms, such as bacteria, was not straightforward<sup>13</sup>, as it required taking into account both surface interaction forces and submolecular mechanical (viscoelasticity, hyperelasticity, damage) responses of the cells to external stresses or strains. However, some publications were able to combine the two approaches and propose original ideas about the double layer structure of the *S. cerevisiae* wall<sup>14</sup>.

Mathematical models for plant cells with walls should include not only the features of yeast, such as turgor pressure, wall tension<sup>15</sup>, but also the possibility of dynamic reorganisation of the wall chain network (poroelasticity) and/or water flowing through it. This could mean taking into account the complex and heterogeneous macromolecular structure of the wall with intertwined glucan fibrils. Although many computational models have been developed to describe the intricate fibre networks of planar cell walls<sup>16,17</sup>, the dynamic reorientation of the fibres under strain has rarely been considered in living small unicellular organisms such as yeast. Original models for the mechanics of microcapsules and shells that considered them as elastic membranes provided a theoretical basis for the identification of mechanical parameters

<sup>a</sup> Address, LOMA, Laboratoire Ondes et Matière d'Aquitaine, CNRS, Université de Bordeaux, 354 Cours de la Libération, 33405 Talence, France. E-mail: francoise.argoul@u-bordeaux.fr

<sup>b</sup> Address, IBGC, Institut de Biologie et Génétique Cellulaire, CNRS, Université de Bordeaux, 1 rue Camille Saint-Saëns, 33077 Bordeaux, France.

<sup>c</sup> Address, LVMT, Ecole des Ponts, Université Gustave Eiffel, 77454 Marne la Vallée, France.

<sup>d</sup> Address, Université Gustave Eiffel, MAST-EMGCU, 77454 Marne la Vallée, France.

Running title: Models for yeast elastic flat compression

from single cell experiments on yeast<sup>18</sup>.

As these early models did not include the effect of turgor pressure, they were not suitable for analysing large deformations. More recently, turgor pressure has also been introduced into such models<sup>20–22</sup> and compared with single cell compression on yeast cells.

In this work, we combine plane-plane AFM compression experiments of single yeast cells with a refined non-linear analysis of force-indentation curves, based on a multiscale methodology. In section 2 we describe the experimental methods, the AFM force-indentation curves calibration, their filtering and correction for further analysis. The force versus displacement curves were corrected by cantilever stiffness, filtered, and derivated to extract different characteristics such as scaling law exponents, effective tension, dissipative loss. This study required a quite large number of force curves to reach a statistical relevance of the mechanical parameters that were extracted from them. Comparing different compression velocities, we conclude that for the depth of compression performed in this study (limit of small deformations), these cells behave essentially as elastic shells<sup>20</sup>. The strength and the originality of our approach relies on a careful computation of the force-displacement curve derivatives, described in section 2.4.

Thanks to a multi-scale analysis of the force curves, we demonstrate that the force curves do not follow simple power laws since the force curve scaling exponent  $\alpha_{eq}$  is not constant but follows a non-monotonous function with the compression distance. Interestingly, this exponent crosses a maximum value at a specific distance which can be compared to a characteristic scale of the cell wall sub-layers. Inspired from the different models proposed in the literature for elastic spheres and shells, we generalize Bonilla and co-authors approach<sup>23</sup> by considering in section 3 the possibility of non-integer scaling laws for the force-displacement curves and we propose simple bi-component elastic models that reproduce fairly well the experimental behavior. The compression experiments were performed at different scan velocities simultaneously to the proliferation of yeasts, keeping the same culture medium, we have selected for illustration here those performed in lactate based synthetic medium. In the last section 4, we discuss our experimental results under the light of the bi-component elastic models introduced in section 3, in particular those including a self-cancelling sub-layer, suggesting not only that the fibrillar structure of the wall could produce its soft-glassy or power-law behavior (nonlinear elasticity)<sup>24</sup> but also that one of the component of the wall (presumably the mannoprotein outer layer) could be completely compressed to reveal the mechanical stiffness of the underlying glucan-chitin network.

## 2 Materials and Methods

### 2.1 Yeast cell cultures and growth survey

The *Saccharomyces cerevisiae* strain BY4742 (WT) ((MAT $\alpha$ ; his3 $\Delta$ 1; leu2 $\Delta$ 0; lys2 $\Delta$ 0; ura3 $\Delta$ 0)<sup>25</sup> (Euroscarf) was used in this study. Cells were grown aerobically at 23 °C in a synthetic minimum medium (SMM): yeast nitrogen base 0.175% (BD Difco SKU 233520) without amino-acids<sup>26</sup>, KH<sub>2</sub>PO<sub>4</sub> 0.1% (WMR), (NH<sub>4</sub>)<sub>2</sub>SO<sub>4</sub> 0.5% (WMR), Casein hydrolysate 0.2%

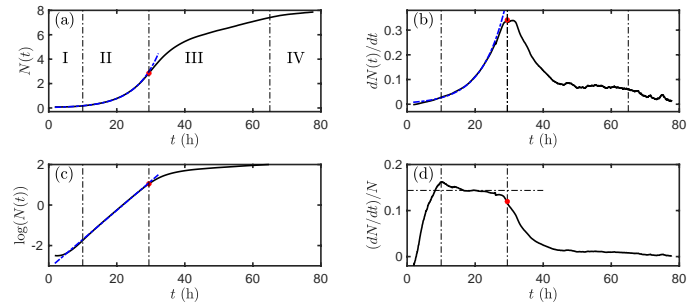


Fig. 1 (a) Plot of the biomass versus time  $N(t)$ . (b) Derivative  $dN/dt$  of the biomass. (c)  $\log(N(t))$ . (d)  $d\log(N(t))/dt$ . Culture medium: SMMLAC. I. Latence phase. II. Growth phase. III. Transition phase. IV. Stationary phase.

(Merk) with sodium-L-lactate 2% (Sigma-Aldrich) and Bactopeptone 1% (Difco) (noted here SMMLAC medium). The choice of synthetic media was guided by our tests in enriched media, such as yeast extract-peptone-dextrose with lactate where we observed a drastic reduction of the adhesion of yeast cells on poly-L-lysine treated surfaces, probably due to the saturation of the positive charges of this layer by negatively charged polypeptidic chains dispersed in the culture media. The culture medium was systematically sterilized by autoclaving at 120°C with 1 bar pressure for 20 minutes. Three amino acids (adenine, uracil and tryptophan) filtered at 0.2  $\mu$ m were added to SSM after autoclaving.

Growth was recorded continuously with a home-designed opto-fluidic (600 nm wavelength) batch reactor<sup>27,28</sup>. This opto-fluidic system was calibrated at the same wavelength (600 nm) with a Shimadzu UV-300 spectrophotometer with both 1 mm and 10 mm cuvettes at each stage of the preparation of the yeast sample (two precultures followed by the real time culture recording in the batch reactor). The two precultures were respectively (i) a first growth on solid agar gel in a petri dish, containing YPD (rich glucose medium: KH<sub>2</sub>PO<sub>4</sub> 0.1% (WMR), (NH<sub>4</sub>)<sub>2</sub>SO<sub>4</sub> 0.12% (WMR), yeast extract 1% (Difco), glucose 2% (Sigma-Aldrich) and (ii) an incubation for 12 to 24 hours at 30°C under constant stirring of two CFUs sampled from the first preculture (i), diluted in 4 mL of the selected culture medium (SMMLAC). Prior to each spectrophotometric measure of absorbance before and after cultures, the solution was homogenized (vortexed) for 30 s at 2100 rpm.

A typical proliferation curve recorded with the opto-fluidic batch reactor in SMMLAC is reported in Fig. 1. The different growth phases can be distinguished from the different representations of  $N(t)$ . The inflexion point of the curve  $N(t)$ , corresponds to the maximum of  $dN/dt$  (red dot in Fig. 1) marks the transition from the growth phase II to the transition phase III. The Boundary line between the phase I and II is estimated from the residues of a linear fit of  $\log(N(t))$  versus  $t$ . The yeast samples which have been used here were selected in the growth phase II exclusively.

### 2.2 Coverslip roughening and poly-L-lysine coating

Because walled cells such as yeast are non motile and do not have an adhesion machinery equivalent to mammal cells, adhesive or structured surfaces have been proposed to facilitate

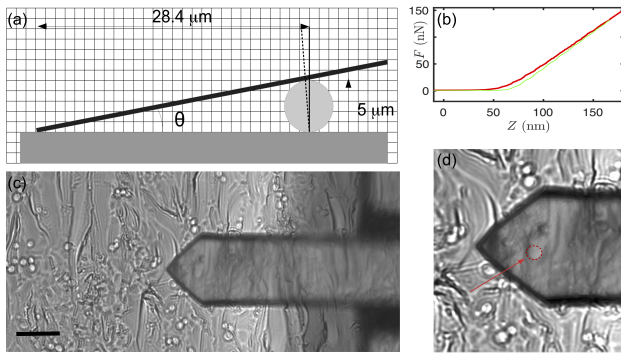


Fig. 2 (a) Schematic of a tipless AFM cantilever in contact with a sphere (lateral view). Given the cantilever tilt angle ( $\theta = 10^\circ$ ), good yeast cell candidates for AFM are selected close enough (typically  $< 28\mu\text{m}$ ) to the cantilever edge. (b) Force curves on a flat glass surface. Red lines: loading scans, green lines: unloading scans. Scan velocity:  $1\ \mu\text{m/s}$ . (c) Image of the tipless AFM cantilever with yeast cells immobilized on a roughened glass plate coated with a poly-L-Lysine layer. (scale bar:  $20\mu\text{m}$ ). (d) zoom of (c) highlighting in red a round yeast cell underneath the cantilever.

their immobilization, such as filter membrane pores<sup>29</sup>, negatively charged groups (imide, lysine, silanes)<sup>30</sup>, microstructured PDMS stamps<sup>31</sup> or glycoproteins (concanavaline (ConA))<sup>32,33</sup>.

The aim of our surface treatment protocol was twofold. In a first step the glass was grooved to prevent lateral sliding of the yeasts with small trenches. Then the grooved glass surface was coated with poly-L-lysine to fix the yeasts to the surface.

**Glass grinding** Round coverslips (diam. 18 mm, Marienfeld ref: 0111580) were first ground with a Buehler EcoMet 250 grinding machine. A grinding disc (grit 360) was magnetically maintained on the rotating platen. The grinding operation consisted in applying on each coverslip with thickness 1.3 to 1.6 mm, a constant and gentle force with a finger tip for 5 minutes at 120 RPM under a constant lubricating water flow. Then the coverslips were rinsed with ultrapure water flow for several seconds, then with ethanol. Finally, the coverslip was let to bathe in a 2% Hellmanex (Hellma) solution overnight and rinsed in ultrapure water then ethanol the next day.

**Coverslip coating with poly-L-lysine** The grooved coverslip was plasma treated for 20 minutes to ensure the hydrophilicity of its surface. It was positioned on the bottom glass of a 35 mm diameter petridish (Fluorodish FD35-100). A drop of poly-L-Lysine (0.01% in water - Sigma-Aldrich 25988-63-0) was deposited on its surface to cover it almost entirely (approx.  $50\ \mu\text{L}$ ). The system petri+glass was incubated for at least 1h at  $37^\circ\text{C}$ . All the following steps were performed at room temperature ( $23^\circ\text{C}$ ). The coverslip was rinsed with a PBS solution and placed in another petri dish filled with 3 mL of SMMLAC with the yeast cells for AFM compression experiments.

### 2.3 AFM operation

AFM experiments were performed on a JPK CellHesion 200 (now commercialised by Bruker Corp. MA - USA). Tipless HQ-NSC36 cantilevers (MikroMasch - Estonia, commercialised by Nanoand-

more) with Au/Cr coating (30-20 nm layers) were used. From the three cantilevers (width  $32.5\mu\text{m}$ , thickness  $1 \pm 0.5\ \mu\text{m}$ ), the middle and stiffer one (B) was used for this study with nominal spring constant  $k=2\ \text{N/m} \pm (0.2 - 9\ \text{N/m})$ , length  $L=90\mu\text{m}$  and resonance frequency in air:  $f_R = 130 \pm 90\ \text{kHz}$ . Flat microcantilevers were chosen for several reasons: (i) to avoid twisting, sliding or torsional effects as the cantilever surface approaches the yeast surface, (ii) to limit off-centre shearing effects that occur when the indenter tip size is smaller than the cell size, as this off-centre shearing produces additional shearing effects on the cell.

### AFM calibration

The calibration of the AFM tips was performed in two steps: (i) a sensitivity and (ii) a spring constant calibration<sup>34</sup>. The sensitivity step (i) was estimated by performing loading-unloading force curves on a clean glass surface. Typical sensitivity values were estimated for HQ-NSC36 cantilevers of  $18 \pm 0.5\ \text{nm/V}$ . The thermal noise measurement method (step (ii)) was based on the equipartition theorem and the dynamic spring constants were corrected as described in<sup>35,36</sup> to obtain the static spring constants (correction factor chosen for rectangular cantilevers:  $0.8197^{37}$ ). Mean spring constants estimated in air for NSC36 flat cantilevers were  $5\ \text{N/m}$  for tips B and  $5.5 \pm 1\ \text{N/m}$  in liquid. Calibration of the cantilever was repeated before each experimental sequence (approximately 2 hours in length). The difficulty of focusing the AFM diode laser at the edge of this smaller cantilever with reproducibility required that the calibration be double-checked each time. Interestingly, although the cantilever was deliberately aimed at individual yeast cells to collect force curves, some of them escaped the zone and instead left a measurement on the glass surface. This provided us a few force curves on glass for each cantilever, from which we checked and corrected, if necessary, the cantilever spring constant (static spring constant).

### Yeast cell imaging under the AFM cantilever

The JPK CellHesion 200 scanner head was coupled to an inverted microscope (Olympus IX71). Two imaging modes were implemented on this device, a transmission mode and a reflexion mode<sup>38</sup>. We notice in Fig. 2(c,d) that the cantilever looks as if it were transparent, which is not true. Surprisingly, we can also distinguish the yeast bodies below the tip of the cantilever, although with less contrast. In our setup, the light reflected from the bottom of the cantilever serves as a secondary light source from which we recover the image of the yeast cell under the cantilever (indicated by a red arrow in Fig. 2(d)). Most correlative imaging studies for AFM-based cell mechanics have focused on fluorescence microscopy<sup>39</sup>. However, the labelling of cellular components with fluorophores often leads to artefacts, such as instability and temporal decay of the staining due to photobleaching, limitation of the labelling to specific fractions (targeted proteins, membrane elements, DNA...) of the cells or tissues, laser degradation for longer investigations. Fluorescent staining may also have a potential impact on the energetic metabolism of cells and consequently on cell mechanics, which consume large amounts of ATP<sup>40</sup>. In contrast, in this study, the cells' state is preserved

as much as possible during their transfert to AFM for mechanical testing.

### AFM force curve collection from living yeast samples

A sample volume of between 20 and 80  $\mu\text{L}$  was pipetted from the yeast batch reactor and diluted in a 3 mL volume of SMMLAC culture medium to give, on average, a single yeast under the AFM cantilever probe surface ( $30 \times 30 = 900 \mu\text{m}^2$ ). This corresponds to approximately  $10^6$  yeasts on the  $9 \text{ cm}^2$  surface of the glass coverslip. It is important to note that during the growth phase most of the cells are budding and therefore appear as doublets under the microscope. The solution was gently stirred by pipetting back and forth a few times before being transferred to the AFM reservoir. The yeasts were allowed to sediment and adhere to the coverslip surface for 10 minutes. We avoided vortexing the cell samples for transfer to the AFM in order to keep them in a similar environment (growth phase) as they were in the batch reactor, we can also note in Fig 2 small groups of cells (two doublets could also appear under the microscope) suggesting that mother and daughter cells remained close or in interaction for one or two cycles.

Constant velocity  $Z$  ramps were performed with AFM, for both loading (red line) and unloading (green line) curves without delay interval (Figs 2 and 3). Note that for simplicity we will use the term force curve in place of force-displacement curve. Six scan velocities were used for each cell :  $0.1 \mu\text{m/s}$  (2),  $0.5 \mu\text{m/s}$  (5),  $1 \mu\text{m/s}$  (5),  $5 \mu\text{m/s}$  (5),  $10 \mu\text{m/s}$  (5) and  $16 \mu\text{m/s}$  (5), giving a total of 27 force curves. Three separated samples were collected from the growth phase (see Fig. 1)) giving a total of  $3 \times 13$  cells, with the same velocity ramps protocol for each, that is  $3 \times 13 \times 27 = 1053$  force curves in the growth phase. This experiment in SMMLAC was repeated four times, giving a total of  $4 \times 1053 = 4212$  force curves that were corrected, filtered and analysed in this study. The sampling frequency of the force curves was adjusted for each velocity to keep  $\delta Z$  close to  $0.1 \text{ nm} \pm 0.003$ . This required therefore a greater sampling frequency for larger scan velocities, from 1 kHz ( $0.1 \mu\text{m/s}$ ) to 160 kHz ( $16 \mu\text{m/s}$ ). This choice was done to keep the same spatial resolution for the force curves for the computation of their derivatives  $dF/dZ$  and  $d^2F/dZ^2$ .

### 2.4 Force curves derivatives

The continuous wavelet transform (CWT) is a mathematical technique introduced in signal analysis in the 1980s<sup>41,42</sup> and since then applied in many contexts, from sound and vibrations in physics and engineering, economics, finance, earthquakes to music or physiological signals. With the norm  $\mathcal{L}^1$ , the one-dimensional wavelet transform of a signal  $F(x)$  reads:

$$\mathcal{W}_\psi[F](b, s) = \frac{1}{s} \int_{-\infty}^{+\infty} F(x) \psi^* \left( \frac{x-b}{s} \right) dx, \quad (1)$$

with  $b$  the position and  $s$  ( $> 0$ ) the scale parameter,  $\psi$  the analysing wavelet,  $x$  is a dummy variable representing  $Z$  or  $\delta$  according to our interests. In the frequency domain, the expression

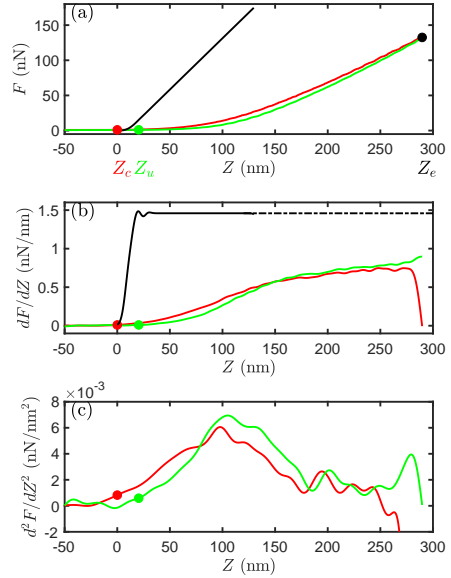


Fig. 3 (a) Force curves  $F(Z)$  recorded on a yeast cell with a tiplless cantilever. (b)  $dF/dZ$ : Derivative of the force curves shown in (a). (c)  $d^2F/dZ^2$ : Second order derivative of the force curves shown in (a). The derivatives in (b) and (c) were computed from wavelet transforms of  $F(Z)$ , using different Gaussian mother wavelet widths  $w_o$  (see text): 14nm for the first derivative, 24.8nm for the second derivative. Red lines: loading scans, green lines: unloading scans. The color and black dots correspond to contact ( $Z_c$  red), end ( $Z_e$  green) and unload ( $Z_u$  black) points. Scan velocity:  $1 \mu\text{m/s}$ . Black lines: loading scans on glass.

of the CWT reads:

$$\mathcal{W}_\psi[F](b, s) = \int_{-\infty}^{+\infty} \hat{F}(f) \hat{\psi}(sf) e^{2i\pi fb} df. \quad (2)$$

We compute the derivatives from the formula:

$$\mathcal{W}_\psi \left[ \frac{dF}{dx} \right] (b, s) = \frac{1}{s} \mathcal{W}_\psi [F](b, s), \quad (3)$$

$$\mathcal{W}_\psi \left[ \frac{d^2F}{dx^2} \right] (b, s) = \frac{1}{s^2} \mathcal{W}_\psi [F](b, s), \quad (4)$$

We choose here the Gaussian function and its derivative for this analysis<sup>42-44</sup>. The interest of this wavelet transform is to perform simultaneously the derivation of  $F$  and a filtering with a smooth function (the mother wavelet). The wavelet analysing window size  $w_o$  is chosen properly to limit the noise introduced by the derivation. Examples of force curve derivatives are shown in Figs. 3 and 4.

### 2.5 Force curves correction with the cantilever stiffness

When the stiffness of the cantilever is not much larger than the rigidity of the tested material, its bending also contributes to the displacement, and it is therefore necessary to perform a correction of the force curves. Eq. (5) shown below was proposed in previous literature pieces<sup>45</sup> and we also provide here original analytical expressions for the corrected force curve derivatives (first and second derivatives). The black force curve shown in Fig. 3(a) was recorded on glass (stiff, non deformable surface)

with a scan velocity of  $1\mu\text{m/s}$ . Except on the very first nanometers after tip-surface contact, this curve is linear (the derivative of this curve shown in Fig. 3(b) is constant). This means that the force-deflection relation follows the Hooke's law:  $F_d = k(d - d_0)$ , where  $k$  is the spring constant of the cantilever and  $d - d_0$  its deflection. We keep  $d_0 \neq 0$ , since there may be a residual flexion of the cantilever. The indentation or deformation  $\delta$  of a soft sample upon compression with the AFM tip reads as the difference between the cantilever displacement  $Z - Z_0$  and the relative deflection of the cantilever  $d - d_0$ :

$$\delta = Z - Z_0 - (d - d_0) = Z - Z_0 - \frac{F}{k}. \quad (5)$$

$Z_0$  correspond to the contact point where  $F = 0$  and  $\delta = 0$ . Except when  $F(Z)$  is linear in  $Z$ , the new coordinate  $\delta$  is a nonlinear function of  $Z$  and the transformation of  $F(Z)$  to  $F(\delta)$  is also nonlinear. Taking the derivative of Eq. (5) with  $F$ , the corrected first derivative of  $F$ :  $dF/d\delta$  is obtained:

$$\frac{dF}{d\delta} = \frac{1}{(dF/dZ)^{-1} - 1/k}. \quad (6)$$

The second order derivatives  $d^2F/d\delta^2$  can also be computed,

$$\frac{d^2F}{d\delta^2} = \frac{d^2F/dZ^2}{\left[ ((dF/dZ)^{-1} - 1/k) \cdot \frac{dF}{dZ} \right]^2}. \quad (7)$$

$dF/dZ$  and  $d^2F/dZ^2$  are first estimated from the experimental force curves with the wavelet transform (section 3) choosing a wavelet width large enough to limit the local fluctuations.

A set of uncorrected (red) and corrected (blue) force curves are shown in Fig. 4. To limit the noise amplification due to a second derivation, the inverse of  $((dF/dZ)^{-1} - 1/k)^2$  was computed with a larger analyzing window width  $w_0 \sim 30$  nm, i.e. one fifth of the total yeast deformation  $\delta$  ( $\sim 150$  nm) (Fig. 4(e) and (f)).

After correction, the force curves and their increase rate may change drastically if the force derivative values become too close to the cantilever stiffness, hence some bias can be introduced by the correction itself. Using stiffer cantilevers implies also a loss of sensitivity, since the cantilever deflection (range of its deformation) is inversely proportional to its stiffness. These curves were captured on two different cells with the same cantilever (with the same 'static' stiffness estimated from glass substrate  $\sim 6.4$  N/m). We will further discuss the peculiarities of these force curves and their derivatives in section 3.

## 3 Results

### 3.1 Evidence of yeast elasticity

Loading and unloading force curves collected from soft glassy materials (including living materials) are rarely superimposed, reflecting that a fraction of the loading (input) work  $W_\ell$  is lost and not recovered in the unloading (output) work  $W_u$ . The dissipation of mechanical work can be written as the ratio<sup>11,46</sup>:

$$D_l = \frac{W_\ell - W_u}{W_\ell} \quad (8)$$

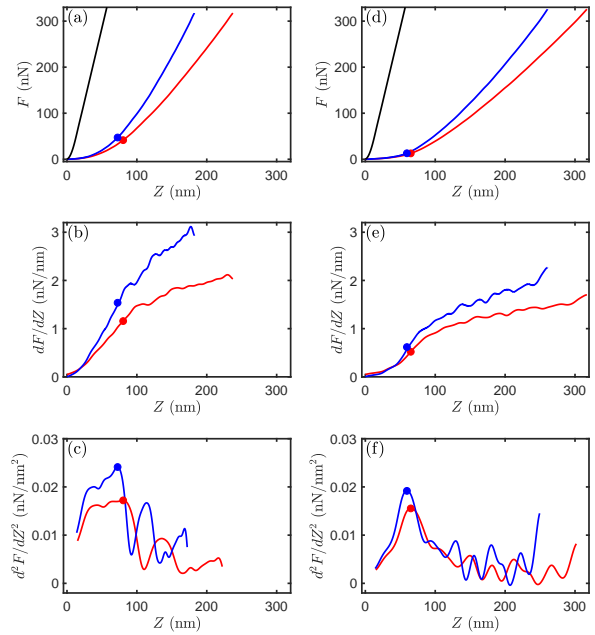


Fig. 4 Illustration of the correction of the force curves with the cantilever deflection. Two examples of force curves collected on two different cells of the same batch are shown in the two column panels. (a,d)  $F(Z)$  (red line) and its correction  $F(\delta)$  (blue line). (b,e)  $dF(Z)/dZ$  (red line) and its correction  $dF(\delta)/d\delta$  (blue line). (c,f)  $d^2F(Z)/dZ^2$  (red line) and its correction  $d^2F(\delta)/d\delta^2$  (blue line). Black lines: cantilever reference force curves recorded on glass.  $d^2F(Z)/dZ^2$  maxima are marked with filled disks. Scan velocity:  $5\mu\text{m/s}$ .

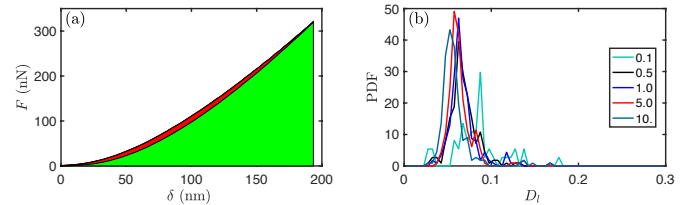


Fig. 5 (a) Load and unload force curves.  $W_u$  (green filled area) and  $W_\ell - W_u$  (red filled area). (b) PDF of  $W_\ell$  values computed from force curves collected from yeast samples in SMMLAC in the growth phase for different scan velocities given in  $\mu\text{m/s}$  in the legend. (collection times: 5h55, 22h35, 27h30 and 30h10).

with

$$W_\ell = \int_c^e F_\ell(\delta) d\delta \text{ and } W_u = \int_e^u F_u(\delta) d\delta, \quad (9)$$

$c$ ,  $e$  and  $u$  are the contact (red), end (black) and unloading (green) points, marked with color dots in Fig. 3. The integrals  $W_u$  and  $W_\ell - W_u$  are color shaded in green and red respectively in Fig. 5(a). Four yeast samples have been analyzed for the reconstruction of the PDF Fig.5, on the same yeast culture in SMM-LAC collected in the growth phase. Five velocities are shown in Fig.5(b), corresponding to different sets of force curves: 70 for  $v = 0.1\mu\text{m/s}$ , 189 for  $v = 0.5\mu\text{m/s}$ , 187 for  $v = 1.0\mu\text{m/s}$ , 182 for  $v = 5.0\mu\text{m/s}$ , 179 for  $v = 10\mu\text{m/s}$ . Note that the broader distribution of  $D_I$  for the smaller velocities ( $0.1\mu\text{m/s}$ ) is due not only to a smaller statistics, but also because this small velocity scans (performed first in the velocity series) are more prone to cells instabilities or rearrangements when the cantilever moves toward the cells.

The coefficient  $D_I$  measures the reversibility of the force curves; when  $D_I$  is close to zero, the load-unload curves can be considered as superimposed and the system behaves as symmetric. As  $D_I$  approaches 1, all the input work is transferred to the sample and not recovered on unloading, the process is fully asymmetric. For mammalian cells, typical values of  $D_I$  are  $> 0.3$  for pre-stressed cells with high stiffness stress fibres, for less adherent unwallled cells larger values of  $D_I$  have been estimated<sup>11</sup>. If dissipation or loss of mechanical work is involved, the coefficient  $D_I$  is expected to increase with scanning speed. The fact that  $D_I$  values remain limited to 0.1 and that  $D_I$  changes little with scanning speed (see Fig.5(b)) is strong evidence that in the small deformation regime yeast cells behave as quasi-reversible systems with little loss of mechanical work. This conclusion validates our choice of multi-component elastic models in the next sections.

### 3.2 Literature models for yeast compression

The force curves, collected from yeast cells with typical diameter  $4\text{-}6\mu\text{m}$ , are quite different from those observed on larger eukaryote cells, not simply because they have a wall driven by internal turgescence but also because they do not use focal adhesion machineries and are more sensitive to solutes and metabolites inter-cell exchanges<sup>47</sup>. We have shown that their response to compression is quasi-elastic, for shallow deformation. Interestingly, the ability of yeast cells to adapt to osmotic or mechanical stress is also dependent on the available source of carbon<sup>48</sup>. A careful examination of the force curve derivatives in Fig. 4(b-f) shows that they do not follow simple power-laws and that standard pressurized shell models (including or not turgescence) would not be efficient for their fitting. Such difficulties were originally discussed by Oliver and Pharr<sup>49</sup> and more recently reported in<sup>23</sup> with illustrations on AFM indentations of *Lolium multiflorum* cells (walled plant cells) and PDMS layers.

However, even if previous theoretical models proposed so far for spherical shape organisms compression do not reproduce what we have observed, they nevertheless bring a theoretical framework that guide our experiment interpretation. We report here rapidly those which seem to us the most relevant. If the yeast cells were made of plain and homogeneous material, the

compression force would be expressed from the Hertz theory as:

$$F(\delta) = \frac{4E}{3(1-\nu^2)} \sqrt{R_0} \left[ \frac{\delta}{2} \right]^{3/2} = \frac{4E}{3(1-\nu^2)} R_0^2 \left[ \frac{\delta}{2R_0} \right]^{3/2}, \quad (10)$$

$R_0$  is the radius of the sphere before compression,  $\nu$  is the Poisson coefficient,  $E$  is the Young modulus.  $\varepsilon = \delta/(2R_0)$  is the relative deformation of the sphere. The scaling exponent  $\alpha_{eq}$  would be  $3/2$ . Except in the very first part of the compression where  $\alpha_{eq}(\delta)$  increases from 1 to  $\alpha_m$ , in a very limited interval of  $\delta$  values, this scaling does not appear in our measures. At the very beginning of the compression (for  $\delta \lesssim 10\text{nm}$ ), the force curves could perhaps be approximated by Eq. (10) and a ‘small-regime’ Young modulus could be estimated. At larger compression this approximation is no longer valid.

The implication of different regimes was mentioned quite early for spherical shallow shells compression. When the compression force is radially localized and points inwards, two regimes were suggested by Landau and Lifzhitz<sup>50</sup> and formalized by Pogorelov<sup>51</sup>. Pogorelov demonstrated that when the force is small, the deformation is localized near the point of application and grows linearly with the force, whereas when the force is large, a circular fold around the point of application appears and the displacement becomes quadratic with the applied force (buckling of the shell). The transition between the two regimes is continuous<sup>52</sup>:

$$\begin{aligned} F &\sim \frac{Eh^2}{R_0} \delta, \text{ for } \delta \ll h, \\ F &\sim \frac{Eh^{5/2}}{R_0} \delta^{1/2}, \text{ for } \delta \gg h. \end{aligned} \quad (11)$$

More recently, Lulevich and co-authors<sup>18</sup> proposed another model for microcapsule deformation that includes two contributions respectively an elastic stretching energy and a bending energy. They did not consider the limit where buckling may be involved. They modelled the deformation of microcapsules (radius  $R_0$ ) with solid spheres ( $R_S$ ), and obtained the total reaction force (load) for  $R_S \gg R_0$ :

$$F(\varepsilon) = \lambda_B E \varepsilon^{1/2} + \lambda_S E \varepsilon^3, \quad (12)$$

where the two prefactors  $\lambda_b = \frac{\pi}{2\sqrt{2}} h^2$  for the bending energy and  $\lambda_S = 4\pi h R_0$  for the stretching energy, with  $h$  is the thickness of the microcapsule,  $E$  its Young modulus,  $\varepsilon$  its relative deformation  $\varepsilon = \delta/(2R_0)$  scaled by the radius of the microcapsule with no dimension,  $\delta$  being the total compression displacement.

Eq. (12) provides a quantitative argumentation for the change of the scaling exponent which could be produced by two mechanical components placed in parallel (we will come back to this aspect in the next sections). Importantly, this calculation is correct only in the limit of  $\varepsilon \ll 1$ , for the smaller  $\varepsilon$  values the  $1/2$  scaling exponent should be observed, whereas for larger deformations the scaling exponent 3 should be expected. The  $\varepsilon_{co}$  value corresponding to the cross-over  $\varepsilon_{co}$  of these two regimes is estimated from the relation:

$$\varepsilon_{co} = \left[ \frac{(1-\nu)h}{2\sqrt{2}R_0} \right]^{2/5}. \quad (13)$$

Lately, Vella and coauthors proposed another modelling for pressurized (including turgor pressure) spherical shell compression<sup>20–22</sup>, based on nonlinear equations of shallow shell theory<sup>53</sup>. They demonstrated both formally and numerically that the force versus deformation crosses over between two limit regimes, both with exponent 1:

$$\begin{aligned} F &\sim k_1 \delta, \text{ for } \delta \ll h, \\ F &\sim k_2 \delta, \text{ for } \delta \gg h, \end{aligned} \quad (14)$$

with  $k_1 \simeq \pi p R_0 / \log(2\tau)$ ,  $k_2 \simeq \pi p R_0$ ,  $\tau = \frac{1}{2} \sqrt{3(1-\nu^2)} p R_0^2 / (E h^2)$ ,  $p$  the pressure drop.

### 3.3 Force curve examination and power-law identification

Definitely, standard methods, based on predefined power laws (related to cell and indenter geometries) that were proposed for living cells in the past decade show limitations for yeast cell compression with flat cantilevers<sup>6,43,44,54–57</sup>. However, we take advantage here of our previous expertise on multi-scale analysis for computing force derivatives and, based on analytical arguments, we generalize the MRA approach<sup>23</sup> to design models of minimal dimension that reproduces fairly well the force curves.

If we come back to Fig. 4, we observe two regimes in these corrected force curves, a first regime with a fast increase of the force derivative, corresponding to a greater curvature of  $F(\delta)$  and a second regime with a slower increase of the force derivative. Rarely, we could observe that  $dF/d\delta$  converges to a horizontal plateau. Interestingly, the correction of the force curves (Eqs (5) (6) and (7)) does not cancel completely this slowing down (Fig. 4(b,d)), the force derivative remains much below the cantilever stiffness. There must be another mechanism, hopefully due to the cell wall, which produces this change during the compression process. We use the maxima of  $d^2F/d\delta^2$  to identify numerically these transitions points (filled colored disks in Fig. 4). The value of the first derivative of the force at this transition point corresponds to a turnover tension undergone by the cell wall before switching to a second compression regime. We will call this quantity an *effective surface tension*. At larger deformation, beyond this transition, different mechanisms can contribute to the slowing down of the force derivative increase; (i) a local distension of the wall fibers producing a shear thinning of the wall, (ii) a perfusion of liquid out of the cell that could deflate progressively the cell and decrease its internal pressure (poro-elasticity of the cell wall). All these processes occur beyond a given deformation, which however remains below the wall thickness typical value (100 to 150 nm). The position of this transition  $\delta_T$  will be used together with the force derivative  $dF/d\delta|_{\delta_T}$  as mechanical markers for these cells. Noticeably, these experiments were performed in the very small deformation limit, purposely to avoid any large scale rupture and to keep the cells alive. We define  $dF/d\delta|_{\delta_T}$  as an effective tension of the cell wall at which this switch occurs.

The  $\log(F)$  versus  $\log(\delta)$  plot shown in Fig. 6(d) highlights the mechanical transition suggested in previous section. Clearly, it is necessary to characterize the local slopes of these curves and their change with the deformation variable  $\delta$ . Assuming that the force scales in a finite range of  $\delta$  as:  $F(\delta) \propto \delta^{\alpha_{eq}}$ , then the local

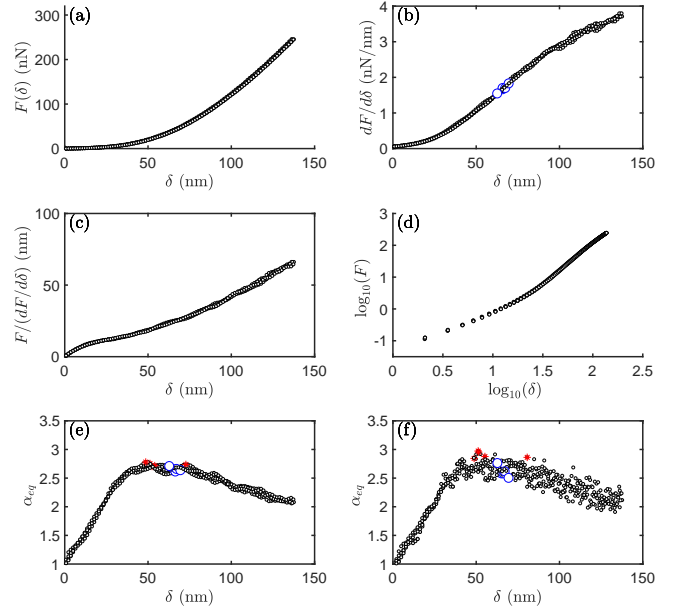


Fig. 6 Extraction of the  $\alpha_{eq}$  exponent values from force curves. (a) Force curves  $F(\delta)$ , after correction for cantilever deflexion. (b)  $dF/d\delta$ . (c) Ratio  $F(\delta)/(dF/d\delta)$  (Eq. (16)). (d)  $\log_{10} F$  vs  $\log_{10} \delta$ . (e)  $\alpha_{eq}(\delta)$  computed from linear fitting the ratio  $F(\delta)/(dF/d\delta)$ . (f)  $\alpha_{eq}(\delta)$  computed from log-log fitting  $F(\delta)$ . Scan velocity  $1\mu\text{m/s}$ . The points corresponding to the local maxima of  $\alpha_{eq}(\delta)$  and  $d^2F/d\delta^2$  are reported with red stars and blue circles respectively.

derivative of  $F$  should scale as  $dF/d\delta \propto \alpha_{eq} \delta^{\alpha_{eq}-1}$ , which gives a simple scaling law for  $F/(dF/d\delta)$ :

$$F/(dF/d\delta) = \alpha_{eq}^{-1} \delta. \quad (15)$$

It can be easily deduced that:

$$\alpha_{eq} = (dF/d\delta)\delta/F. \quad (16)$$

We have therefore two possibilities for computing the local exponent  $\alpha_{eq}$ , (i) fitting the  $\log(F)$  versus  $\log(\delta)$  curves or (ii) fitting  $F/(dF/d\delta)$  versus  $\delta$  curves. Both methods were tested in parallel. The second representation offers the advantage to perform a linear fit with equally spaced  $\delta$  data points, giving the same weight to all the points. For the  $\log(F)$  versus  $\log(\delta)$  fits, we had to perform an interpolation of the  $\log \delta$  points to get them equally spaced.

If there exists a range of scale in which the force curve  $F(\delta)$  scales with a single exponent, as suggested by the experimental bi-logarithmic force curves (Fig. 6(d)), we should get this exponent value with either of these fitting procedures. However, comparing the  $\alpha_{eq}(\delta)$  plots obtained with these two methods (Fig. 6(e,f)), we observe that the bilogarithmic fits give much more noisy estimations than the  $F(\delta)/(dF/d\delta)$  ratio.

We have therefore preferred the extraction method based on the  $F(\delta)/(dF/d\delta)$  ratio for its greater robustness. Interestingly, because  $dF/d\delta$  is also computed through the wavelet filtering (Eq. (3)), it smooths the computation of  $F/(dF/d\delta)$ .

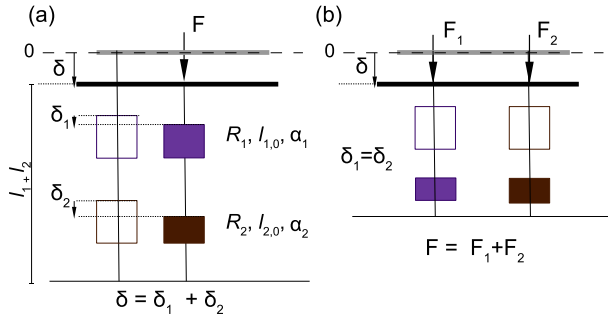


Fig. 7 Schematic of the system with two mechanical components (1) and (2) in series (a) and in parallel (b).

The shape of  $\alpha_{eq}(\delta)$  is very interesting, since it highlights the fact that  $\alpha_{eq}$  is not constant; in a first stage  $\alpha_{eq}$  increases sharply from 1 and reaches a plateau (more or less flattened) and in a second stage it decreases more softly.  $\alpha_{eq}(\delta)$  is asymmetric, the two regimes which are involved before and after the transition are therefore expected to be of different nature. We note  $\delta_{\alpha_m}$  the abscissa are which  $\alpha_{eq}(\delta)$  is maximum. It can be estimated from each force curve, in Fig. 6(e), its position is marked by red stars on 5 consecutive force curves recorded from the same cell with the same scan velocity (1  $\mu\text{m/s}$ ). The local maxima of  $d^2F/d\delta^2$ ,  $\delta_T$  are also marked by blue circles. These two transition points are close to each other, but we cannot conclude here that they overlap.

We have pointed out three types of models in section 3.2, one model (Eq. (10)) with a constant exponent, one model with two exponents giving the force as the sum of two power laws (Eq. (12)) and two models with two limit regimes with a different effective scaling exponent at very small deformation than at large deformation (Eqs (11) and (14)). Surprisingly, the force curves obtained from these compression experiments are very different from these theoretical predictions. However, if we examine closely the predictions of Vella and co-authors<sup>20–22</sup>, we find that they demonstrate the occurrence of two distinct power law regimes with the same exponent 1, which would suggest that in the intermediate regime the effective exponent  $\alpha$  is no longer 1 and that it must make a non-linear incursion between these two limits. This model is actually the closest representation of our experimental configuration, since it considers not only the planar compression but also the pressurisation of the shell. It would be interesting to calculate the  $\alpha_{eq}$  introduced here from their simulated data and compare it with our experimental estimates.

Here we design multi-component elastic systems, in line with Bonilla and co-authors<sup>23</sup> multi-regime analysis (MRA) elaborated from a general multi-resistor mechanical system for fitting the experimental data. Two configurations are considered, a system with two components in series (Fig. 7(a)) and a system with two components placed in parallel (Fig. 7(b)).

### 3.4 Association of two standard elastic elements

#### 3.4.1 Parallel association

The ‘parallel’ system involves two mechanical components placed in parallel (Fig. 7(b)). Each element follows a generalized stress-to-strain relation. We have:

$$\begin{aligned} F_1 &= R_1 \left( \frac{\delta}{\ell_{1,0}} \right)^{\alpha_1}, \\ F_2 &= R_2 \left( \frac{\delta}{\ell_{2,0}} \right)^{\alpha_2}, \\ F &= F_1 + F_2, \quad \delta = \delta_1 = \delta_2. \end{aligned} \quad (17)$$

$F$  is the compression force,  $R_1$  and  $R_2$  are scaling factors with the dimension of forces,  $\ell_{1,0}$  and  $\ell_{2,0}$  are scaling lengths,  $\delta_1$  and  $\delta_2$  are the displacement of each component.  $\delta_i = 0$  when  $F = 0$ . We have introduced factors  $R_i$  and  $\ell_{i,0}$ ,  $i = 1, 2$  for each component, not only to keep the homogeneity of Eqs (17) whatever the exponents  $\alpha_1$  and  $\alpha_2$ , but also to introduce the characteristic size and strength of each component.

The computation of  $dF/d\delta$  is immediate:

$$\frac{dF}{d\delta} = \frac{dF_1}{d\delta} + \frac{dF_2}{d\delta} = \frac{\alpha_1}{\delta} F_1 + \frac{\alpha_2}{\delta} F_2. \quad (18)$$

$\alpha_{eq}$  introduced in Eq. (16) can be computed as:

$$\alpha_{eq} = \frac{\alpha_1 F_1 + \alpha_2 F_2}{F_1 + F_2} = \frac{\alpha_1 + \alpha_2 F_2/F_1}{1 + F_2/F_1}. \quad (19)$$

Given that

$$\frac{F_2}{F_1} = \frac{R_2(\ell_{1,0})^{\alpha_1}}{R_1(\ell_{2,0})^{\alpha_2}} \delta^{\alpha_2 - \alpha_1} = A \delta^{\alpha_2 - \alpha_1} \quad \text{with } A = \frac{R_2(\ell_{1,0})^{\alpha_1}}{R_1(\ell_{2,0})^{\alpha_2}}, \quad (20)$$

we obtain:

$$\alpha_{eq} = \frac{\alpha_1 + A \alpha_2 \delta^{\alpha_2 - \alpha_1}}{1 + A \delta^{\alpha_2 - \alpha_1}}. \quad (21)$$

If we assume that  $1 \leq \alpha_1 < \alpha_2$ , from Eq. (21) we get the limit values:

$$\lim_{\delta \rightarrow 0} (\alpha_{eq}) = \alpha_1 \quad \text{and} \quad \lim_{\delta \rightarrow +\infty} (\alpha_{eq}) = \alpha_2. \quad (22)$$

With the parallel association of two mechanical components,  $\alpha_{eq}$  increases monotonously from the smallest exponent ( $\alpha_1$ ) to the largest one ( $\alpha_2$ ) (see Fig. 8(d)).

#### 3.4.2 Series association

The ‘series’ system is the sum of two mechanical components placed in series (Fig. 7(a)). The generalized stress-to-strain relations are:

$$\begin{aligned} F_1 &= R_1 \left( \frac{\delta_1}{\ell_{1,0}} \right)^{\alpha_1} \\ F_2 &= R_2 \left( \frac{\delta_2}{\ell_{2,0}} \right)^{\alpha_2} \\ F &= F_1 = F_2, \quad \delta = \delta_1 + \delta_2 \end{aligned} \quad (23)$$

The parameters  $R_1$ ,  $R_2$ ,  $\ell_{1,0}$  and  $\ell_{2,0}$  are defined as above for the parallel model.  $F$  is the compression force.

From Eqs (23), we compute the total displacement  $\delta$  and the derivative of the force  $dF/d\delta$ :

$$\delta = \delta_1 + \delta_2 = \ell_{1,0} \left[ \frac{F}{R_1} \right]^{1/\alpha_1} + \ell_{2,0} \left[ \frac{F}{R_2} \right]^{1/\alpha_2}. \quad (24)$$

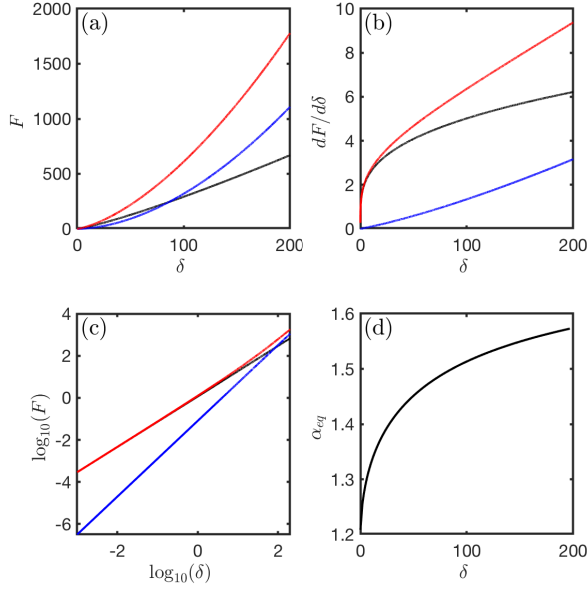


Fig. 8 Force curves predicted by the parallel model Eq. (17). We take  $\alpha_1 = 1.2$ ,  $R_1 = 8$ ,  $\ell_{1,0} = 5$ , and  $\alpha_2 = 1.8$ ,  $R_2 = 0.08$ ,  $\ell_{2,0} = 1$ , to mimic what is observed in experimental force curves. (a) Force displacement curves. (b) Derivatives of the force curves. (c) Force displacement curves in log-log scales. (d)  $\alpha_{eq}(\delta)$  curve computed from the local slope of (c). black lines: component (1), blue lines: component (2), red lines: sum of components.

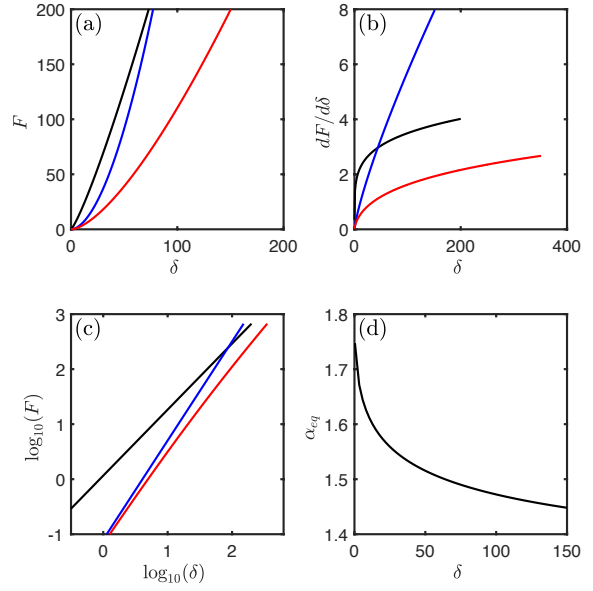


Fig. 9 Force curves predicted by series model Eq. (23). We take  $\alpha_1 = 1.2$ ,  $R_1 = 8$ ,  $\ell_{1,0} = 5$ , and  $\alpha_2 = 1.8$ ,  $R_2 = 0.08$ ,  $\ell_{2,0} = 1$ , to mimic what is observed in experimental force curves. (a) Force displacement curves. (b) Derivatives of the force curves. (c) Force displacement curves in log-log scales. (d)  $\alpha_{eq}(\delta)$  curve computed from the local slope of (c). black lines: component (1), blue lines: component (2), red lines: sum of components.

and

$$\frac{dF}{d\delta} = F / \left[ \frac{\ell_{1,0}}{\alpha_1} \left( \frac{F}{R_1} \right)^{1/\alpha_1} + \frac{\ell_{2,0}}{\alpha_2} \left( \frac{F}{R_2} \right)^{1/\alpha_2} \right] \quad (25)$$

$\alpha_{eq}$  can then be computed from Eq. (15):

$$\frac{\delta}{\alpha_{eq}} = \frac{F}{dF/d\delta} = \frac{\delta_1}{\alpha_1} + \frac{\delta_2}{\alpha_2}, \quad (26)$$

If we replace  $\delta_1 = \delta - \delta_2$ , we get the relation:

$$\frac{1}{\alpha_{eq}} = \frac{1}{\alpha_1} + \frac{\delta_2}{\delta} \left( \frac{1}{\alpha_2} - \frac{1}{\alpha_1} \right). \quad (27)$$

It is possible in that case of series association to express  $\delta_2/\delta$  in function of  $F$ :

$$\frac{\delta_2}{\delta} = \frac{\ell_{2,0} \left( \frac{F}{R_2} \right)^{1/\alpha_2}}{\ell_{1,0} \left( \frac{F}{R_1} \right)^{1/\alpha_1} + \ell_{2,0} \left( \frac{F}{R_2} \right)^{1/\alpha_2}}, \quad (28)$$

or equivalently

$$\frac{\delta_2}{\delta} = \frac{1}{1 + \frac{\ell_{1,0}}{\ell_{2,0}} \left( \frac{1}{R_1} \right)^{1/\alpha_1} \left( \frac{1}{R_2} \right)^{-1/\alpha_2} F^{(1/\alpha_1 - 1/\alpha_2)}}. \quad (29)$$

Assuming that  $1 \leq \alpha_1 < \alpha_2$ , then  $1 \geq 1/\alpha_1 > 1/\alpha_2$ ; or  $1/\alpha_1 - 1/\alpha_2 \geq 0$ . We can calculate the following limits:

$$\text{If } F \rightarrow 0 \text{ then } \frac{\delta_2}{\delta} \rightarrow 1 \text{ and } \frac{1}{\alpha_{eq}} \rightarrow \frac{1}{\alpha_2}, \quad (30)$$

$$\text{If } F \rightarrow +\infty \text{ then } \frac{\delta_2}{\delta} \rightarrow 0 \text{ and } \frac{1}{\alpha_{eq}} \rightarrow \frac{1}{\alpha_1}. \quad (31)$$

In the example of Fig. 9(d), we observe that  $\alpha_{eq}$  decreases monotonously from the largest exponent (here  $\alpha_2$ ) to the smallest one ( $\alpha_1$ ). With the series mechanical model of Eq. (23), this decrease of  $\alpha_{eq}$  is observed for any couple of exponents ( $\alpha_1, \alpha_2$ ). We can conclude that this model cannot either reproduce the bell shape of  $\alpha_{eq}(\delta)$  extracted from the experiments (such as those of Fig. 6(e)).

### 3.5 Self-canceling component

The previous parallel and series two mechanical component systems are not adequate for reproducing the experimental  $\alpha_{eq}$  curves. We were therefore interested in a component that could not be deformed beyond a thickness  $h$  (we take  $h = 30$  nm as example in Fig. 10). In other words, when the displacement  $\delta$  gets close to the value  $h$ , the force diverges and the corresponding mechanical component no longer deforms:

$$F(\delta) = R \left[ \frac{\delta}{\ell_0} \right]^\alpha \frac{1}{h - \delta}, \text{ for } \delta < h. \quad (32)$$

Mathematically speaking  $F$  can be expressed in the sense of distributions as:

$$F(\delta) = F \left[ \frac{\delta}{\ell_0} \right]^\alpha \frac{1}{h - \delta} [H(\delta) - H(\delta - h)], \quad (33)$$

where  $H(\delta)$  is the Heaviside function. This expression is more rigorous from a mathematical point of view, particularly with re-

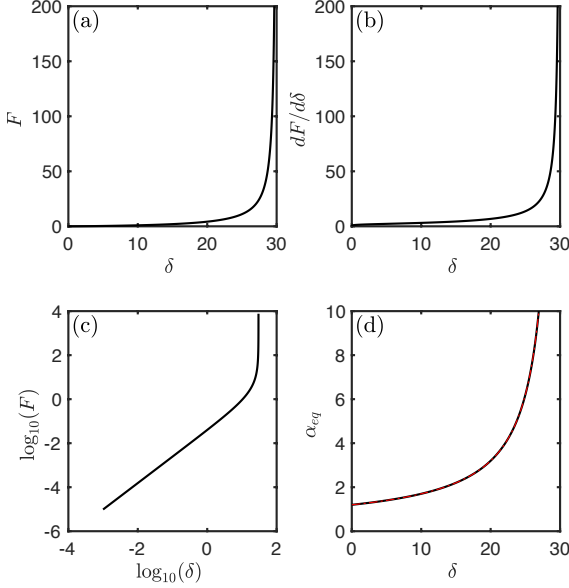


Fig. 10 Force curves computed for a single self-cancelling component Eq. (32).  $\alpha = 1.2$ ,  $R = 8$ ,  $\ell_0 = 5$ ,  $h = 30$ . (a) Force displacement curves. (b) Derivatives of the force curves. (c) Force displacement curves in log-log scales. (d)  $\alpha_{eq}(\delta)$  curve computed from Eq. (35) (black line) and from the local slope of (c) (red dashed line).

gard to discontinuity points of the function  $\delta$  and/or its successive derivatives ( $\delta = 0$ ,  $\delta = h$ ). However, its use leads to more complex calculations, especially with its successive derivatives and with its logarithm, which require Cauchy principal values (see chap. 4 of<sup>58</sup>). We will therefore restrict the following calculations to the case where  $\delta \in ]0, h[$ , for the sake of simplicity.

The first derivative of  $F$  reads:

$$\frac{dF}{d\delta} = \frac{\alpha h + (1 - \alpha)\delta}{(h - \delta)\delta} F. \quad (34)$$

From Eq. (16), we get the relation for  $\alpha_{eq}$ :

$$\alpha_{eq} = \frac{\alpha h + (1 - \alpha)\delta}{h - \delta}. \quad (35)$$

and for the limits at the edges of the interval  $]0, h[$

$$\lim_{\delta \rightarrow h^-} (\alpha_{eq}) = +\infty, \quad \lim_{\delta \rightarrow 0^+} (\alpha_{eq}) = \alpha. \quad (36)$$

We observe that the plot of  $\alpha_{eq}$  versus  $\delta_1$  in Fig. 10(d) diverges when  $\delta \rightarrow h^-$ , in the same way as  $F(\delta)$  and  $dF/d\delta(\delta)$ . This self-cancelling mechanical component is particularly interesting in a formal aspect since if we place it in series with another component, after a given deformation it should no longer contribute to the mechanical response, whereas if we place it in parallel with another component it should impede a further compression for the whole mechanical association. In the first case, it ‘disappears’ from the response and in the second case it monopolizes the mechanical response.

We discuss the parallel association of two elastic components in the supplementary ESI file<sup>†</sup> (Section 1.2) and conclude that this

parallel association of a self-cancelling element with a nonlinear elastic component cannot reproduce what has been observed in our single yeast cell compression experiments. We focus here on the more interesting case of series association.

### 3.5.1 Self-canceling element in series

We consider now the association in series of a self-cancelling element with a standard nonlinear elastic mechanical component. We replace the first relation of Eq. (23) by a self-cancelling element and we get:

$$\begin{aligned} F_1(\delta_1) &= R_1 \left[ \frac{\delta_1}{\ell_{1,0}} \right]^{\alpha_1} \frac{1}{h - \delta_1}, \quad \text{for } \delta_1 < h \\ F_2(\delta_2) &= R_2 \left[ \frac{\delta_2}{\ell_{2,0}} \right]^{\alpha_2}, \quad \text{for } 0 \leq \delta_2, \\ F &= F_1 = F_2, \quad \delta = \delta_1 + \delta_2. \end{aligned} \quad (37)$$

The first derivatives of  $F$  reads:

$$\frac{dF}{d\delta_1} = \frac{R_1}{\ell_{1,0}^{\alpha_1}} \left[ \frac{\delta_1^{\alpha_1 - 1} (\alpha_1 h + (1 - \alpha_1)\delta_1)}{(h - \delta_1)^2} \right] = \left( \frac{\alpha_1}{\delta_1} + \frac{1}{(h - \delta_1)} \right) F \quad (38)$$

and

$$\frac{dF}{d\delta_2} = \frac{R_2}{\ell_{2,0}^{\alpha_2}} \left[ \alpha_2 \delta_2^{\alpha_2 - 1} \right] = \frac{\alpha_2}{\delta_2} F. \quad (39)$$

From Eq. (16) and previous Eqs (38) and (39), we can obtain:

$$\alpha_{eq} = \frac{\delta}{F} \frac{dF}{d\delta} = \frac{\delta_1 + \delta_2}{\frac{\delta_1}{\alpha_1 + \delta_1/(h - \delta_1)} + \frac{\delta_2}{\alpha_2}}, \quad (40)$$

with  $\delta = \delta_1 + \delta_2$ ,  $\delta_1 \leq h$ .

Importantly, in the limit of  $\delta \rightarrow +\infty \gg h$ ,  $\delta_1$  is bounded by  $h$  and  $\delta = \delta_1 + \delta_2$ . It corresponds to  $\delta_2 \rightarrow +\infty$ , then  $\alpha_{eq} \sim \frac{\delta}{\delta_2/\alpha_2} = \alpha_2$ . Therefore  $\alpha_{eq} \rightarrow \alpha_2$  when  $\delta \rightarrow +\infty$ , independently of  $\alpha_2 > \alpha_1$  or  $\alpha_2 < \alpha_1$ .

The limit for  $\delta \rightarrow 0$ ,  $\delta_1 \ll h$  and  $\frac{\delta_1}{h - \delta_1}$  ‘‘small’’, as compared to  $\alpha_1$ :

$$\alpha_{eq} \sim \frac{\delta_1 + \delta_2}{\frac{\delta_1}{\alpha_1} + \frac{\delta_2}{\alpha_2}} = \frac{1 + \frac{\delta_2}{\delta_1}}{\frac{1}{\alpha_1} + \frac{\delta_2}{\alpha_2 \delta_1}}. \quad (41)$$

In the limit  $\delta \rightarrow 0$ , either  $\delta_2/\delta_1 \rightarrow 0$  and then  $\alpha_{eq} \rightarrow \alpha_1$  or  $\delta_1/\delta_2 \rightarrow 0$  and then  $\alpha_{eq} \rightarrow \alpha_2$ .

The transition regime is obtained when intermediate values of  $\delta_1$  become close to  $h$  and  $\delta = \delta_1 + \delta_2 > h$  remains finite; we can write  $\delta_1 = h(1 - \xi)$  with  $\xi \ll 1$  and  $\delta = \delta_1 + \delta_2 = h - h\xi + \delta_2$ . From Eq. (40) we get:

$$\alpha_{eq} = \frac{h - h\xi + \delta_2}{\frac{h(1 - \xi)}{\alpha_1 + (1 - \xi)/\xi} + \frac{\delta_2}{\alpha_2}} \sim \alpha_2 \left( \frac{\delta}{\delta - h} \right) \quad \text{when } \xi \rightarrow 0. \quad (42)$$

It can be noted that when  $\delta \rightarrow h^+$  ( $\delta_1 \sim h$  and  $\delta_2 \rightarrow 0^+$ ),  $\alpha_{eq}$  increases rapidly.

In Fig. 11 we use  $\alpha_1 = 1.2$  and  $\alpha_2 = 1.8$ , as with previous two-mechanical component systems. With the introduction of the self-cancelling element, we observe a similar behavior as the one observed on experimental force curves. The local exponent  $\alpha_{eq}(\delta)$  goes through a maximum value  $\alpha_m$  for  $\delta_{\alpha_m}$ , and the position of this maximum is not precisely  $h$  but is slightly larger than  $h$ . Again this is only an example for which we have chosen realistic values

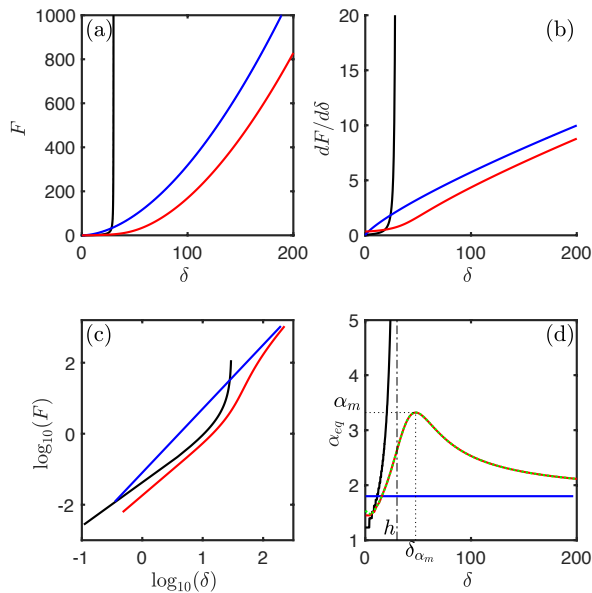


Fig. 11 Force curves computed for a series association of a self-cancelling component and a nonlinear elastic component Eq. (37).  $\alpha_1 = 1.2$ ,  $R_1 = 8$ ,  $\ell_{1,0} = 5$  (black lines) and  $\alpha_2 = 1.8$ ,  $R_2 = 0.08$ ,  $\ell_{2,0} = 1$  (red lines),  $h = 30$  nm. (a) Force displacement curves. (b) Derivatives of the force curves. (c) Force displacement curves in log-log scales. (d)  $\alpha_{eq}(\delta)$  curve computed from Eq. (40) (green dotted line) and from the local slope of (c) (red line).

for  $\alpha_1$ ,  $\alpha_2$  and  $h$ . The asymmetry of the  $\alpha_{eq}(\delta)$  curves is well reproduced also, and from the range of  $\delta$  values reported here we may anticipate that it will converge to the exponent  $\alpha_2$  of the sub-layer (2). We can also conclude that the fact that one of the layer introduces a strong nonlinearity in the compression response of the whole system that we would never obtain by a simple combination of standard power-law mechanical components. The real situation is probably more complex than what we have described in Eq. (37), however it highlights the possibility to use these compression measures not only to validate the existence of mechanical sublayers of the YCW with very different behaviors but also to consider that one of the layer could undergo a drastic change in its response, leading to highly nonlinear behavior, where its original scaling law would break. The scale of the transition phenomena observed in our AFM experiments could correspond the compression limit value of the YCW outer layer.

## 4 Discussion

### 4.1 About experimental investigations

The difficulty of the experimental investigations reported in this paper must first be emphasised. One of the aims of this research is to analyse long-term cell proliferation processes and their relationship to cell mechanics. It should be noted that long-term cultures are not straightforward, such very long experiments were difficult to perform without encountering unpredictable perturbations (spoilage of the samples by environmental agents, temperature drifts of the room air conditioning, temperature instabil-

ities, tubing leaks, evaporation, contamination, loss of computer coupling with the system camera). Considering that each proliferation required a day of pre-culture, the total duration of a single run could reach about 100 h.

The AFM measurements were also very time-consuming, as the collection of force curves could not be automated because cells sometimes escaped from the cantilever. Yeast cells are very small, much smaller than most eukaryotic cells that are typically characterised mechanically with this nanomechanical tool. AFM has a very high sensitivity and can therefore detect even minute perturbations. The yeast cells are not adherent cells, their rounded shape makes their adhesion to a sticky layer more unstable, the experiments performed at low speed (100 nm/s) often implied a small drift or rocking of the cells that we could not analyse properly (Fig. 5(b)).

This work focused on the global compression of yeast cells, which had to remain sufficiently stable in their position to allow measurements to be taken. The valid measurements were not immediately apparent from a visual inspection of the recorded signals, but only after calibration and analysis. This may explain why at least four runs for each condition were required to collect two complete experimental runs for each choice of culture medium.

### 4.2 Comparison of $d^2F/d\delta^2$ and $\alpha_{eq}(\delta)$ curves

In this paragraph, we compare the plots of  $d^2F/d\delta^2$  and  $\alpha_{eq}(\delta)$  and in particular their respective curves and maxima.

In most force curves recorded during AFM compression of single yeast cells, we observed that the curvature of the first order derivative of the force changes from positive below  $\sim 50$  nm to negative above (Fig. 12(b)), corresponding to a local maximum of  $d^2F/d\delta^2$  (Fig. 12(d)).

Remarkably, this transition occurs in the vast majority of flat cantilever AFM compression experiments on yeast cells, independent of culture media and scan velocities. The same is true for the shape of the  $\alpha_{eq}(\delta)$  curves, which does not change much with scan velocity. These observations will allow us, in the following, to average the  $\alpha_{eq}(\delta)$  curves in order to minimise their noisy fluctuations.

Moreover, this local maximum of  $d^2F/d\delta^2$  also seems to correspond to the local maximum of  $\alpha_{eq}(\delta)$  (see Figs 6(b) and 12(e,f)).

Fig. 12(f) compares the profiles  $\alpha_{eq}$  (panel (e)) and the second derivative of the force  $d^2F/d\delta^2$  (panel (d)) as functions of  $\delta$  for the same experiment as that shown in Fig. 6, for three different scan velocities (500, 1000 and 5000 nm/s).

We can observe that the detection of the local maxima of  $d^2F/d\delta^2(\delta)$  is strongly impaired and biased by the fluctuations produced by the derivation method combined to the intrinsic data noise, the black empty circles (maxima of  $d^2F/d\delta^2(\delta)$ ) are systematically slightly larger than the red stars (maxima of  $\alpha_{eq}(\delta)$ ) in Fig. 12(e).

Assuming the weak dependence of the curves  $d^2F/d\delta^2(\delta)$  and  $\alpha_{eq}(\delta)$  on the scan speed, we compute their averages.  $\alpha_{eq}(\delta)$  is plotted with a thicker orange line in Fig. 12(e) and  $d^2F/d\delta^2(\delta)$  is plotted with a thicker orange line in 12(d). Finally,  $\alpha_{eq}(\delta)$  and

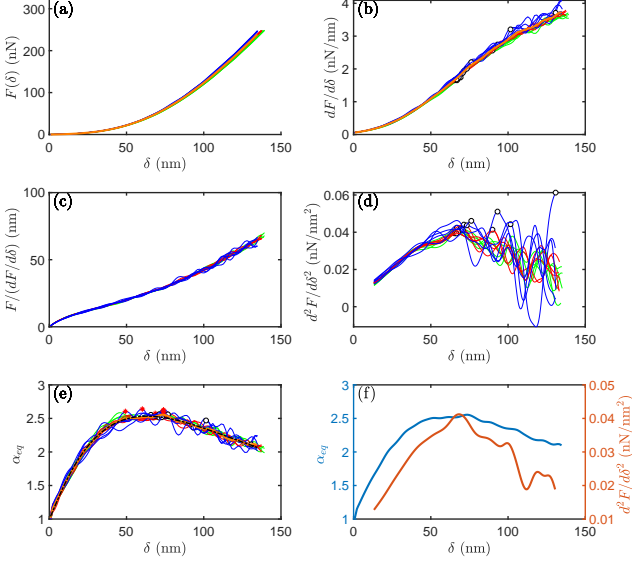


Fig. 12 Analyzing the change of the power law exponent  $\alpha_{eq}$  with parameter  $\delta$ . (a) Corrected force curves  $F(\delta)$ . (b)  $dF/d\delta$ . (c) Ratio  $F(\delta)/(dF/d\delta)$ . (d) Second derivative of the force curve  $d^2F/d\delta^2$ . (e)  $\alpha_{eq}(\delta)$  computed from linear fitting the ratio  $F(\delta)/(dF/d\delta)$ . (f) Comparison of the averaged  $\alpha_{eq}(\delta)$  (blue line) and  $d^2F/d\delta^2$  (orange line) curves. Scan velocities (5 force curves for each): 500 nm/s (green lines), 1000 nm/s (red lines) and 5000 nm/s (blue lines). The averaged curves are plotted with thick orange lines in (b), (d) and (e). The points corresponding to the local maxima of  $\alpha_{eq}(\delta)$  and  $d^2F/d\delta^2$  are reported with red stars and black circles respectively.

$d^2F/d\delta^2(\delta)$  are plotted together in Fig. 12(f).

It can be seen that the averaging of the  $\alpha_{eq}(\delta)$  curves recorded for different speeds reduces the fluctuations, unlike the averaging of the  $d^2F/d\delta^2(\delta)$  curves. Nevertheless, the difficulty remains in correctly identifying the maxima of  $\alpha_{eq}(\delta)$ .

To solve this issue, we introduce an analytical function  $\Phi(\delta)$  that facilitates this identification (dashed black line plotted in Fig. 12(e)). The definition and illustration of  $\Phi(\delta)$  can be found in the electronic supplementary information (EIS) file<sup>†</sup>: section 1.1: *Modelling and fitting  $\alpha_{eq}(\delta)$  curves*. This function  $\Phi(\delta)$  is a sum of two well-documented functions,  $f(\delta)$  and  $g(\delta)$ , and is used as a support for the local maximum of the  $\alpha_{eq}$  identification; it is not intended to have any mechanical meaning here. The black dashed line in Fig. 12(e) is calculated by fitting the mean  $\alpha_{eq}(\delta)$  curve (thick orange line) with  $\Phi(\delta)$ . The local maximum is then estimated numerically from the fitted function  $\Phi(\delta)$ . Once the  $\delta$  position  $\delta_{\alpha_m}$  corresponding to the maximum of  $\alpha_{eq}$  has been estimated,  $\delta_{\alpha_m}$  and  $\alpha_m$  are stored and the corresponding force derivative  $dF/d\delta|_{\alpha_m}$  is interpolated from the mean curve  $dF/d\delta$  as a function of  $\delta$  and stored.

Another technique for estimating the local maximum of  $\alpha_{eq}$  is proposed here. To do this, we analytically derive  $\alpha_{eq}$ , defined in eq.(16), as a function of  $\delta$ . This is easy to find:

$$\frac{d\alpha_{eq}}{d\delta} = \frac{\alpha_{eq}}{\delta} - \frac{\alpha_{eq}^2}{\delta} + \frac{\delta}{F} \frac{d^2F}{d\delta^2}. \quad (43)$$

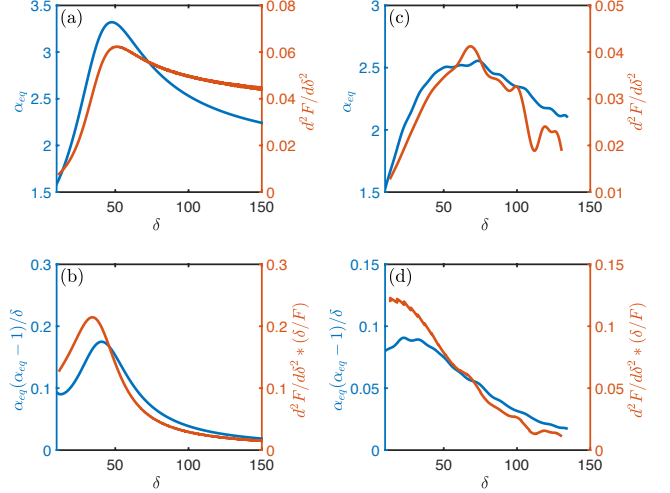


Fig. 13 Comparison of  $\alpha_{eq}(\delta)$  (in blue) with  $d^2F/d\delta^2$  (in orange) curves for (a) the numerical data of the previous self-canceling element in series illustrated in Fig. 11 and for (c) the experimental data illustrated in Fig. 6. Comparison of  $\frac{\alpha_{eq}}{\delta} - \frac{\alpha_{eq}^2}{\delta}$  (in blue) with  $\frac{d^2F}{d\delta^2} \frac{\delta}{F}$  (in orange) curves for (b) the numerical data of the previous self-canceling element in series illustrated in Fig. 11 and for (d) the experimental data illustrated in Fig. 6.

And when

$$\frac{\alpha_{eq}}{\delta} - \frac{\alpha_{eq}^2}{\delta} = \frac{\delta}{F} \frac{d^2F}{d\delta^2}, \quad (44)$$

then  $\frac{d\alpha_{eq}}{d\delta} = 0$ .

Previous equation (44) can allow to estimate graphically the coordinates of local maximum of  $\alpha_{eq}(\delta)$ :  $\delta_{\alpha_m}$  and  $\alpha_m$ . This procedure was applied first to the numerical data of the previous self-canceling element in series illustrated in Fig. 11 and then to the experimental data illustrated in Fig. 6.

The results for both cases are shown in Fig. 13(b) and (d), where the two curves  $(\alpha_{eq} - \alpha_{eq}^2)/\delta$  and  $\frac{d^2F}{d\delta^2} \frac{\delta}{F}$  are plotted as a function of  $\delta$ , respectively. It can be observed in Fig. 13(b) and (d) that these curves intersect at a point whose abscissa is close to that of the maximum of  $\alpha_{eq}$ . The fact that the two curves intersect at a point with an abscissa close to the maximum of  $\alpha_{eq}$  reinforces our approach of modelling the indentation force as a function of  $\delta$  by a power law with a non-constant exponent that depends on  $\delta$ . Finally, from these observations, we can conclude to a first approximation that the two points  $\delta_T$  and  $\delta_{\alpha_m}$  (corresponding respectively to a local maximum of  $d^2F/d\delta^2(\delta)$  and  $\alpha_{eq}(\delta)$ ) can be considered as similar and that we can choose either method (second derivative of the force or calculation of the  $\alpha_{eq}(\delta)$  curve) to identify them from the force curves.

This is an important clue for understanding how the YCW structure changes at  $\delta_{\alpha_m}$ . From our discussion above, we can consider the value  $\delta_{\alpha_m}$  as a transition point where the wall tension increase slows down. This behavior must be related to a switch in the wall structure, that reverses its behavior (maximum of  $\frac{d^2F}{d\delta^2}$ ). Imagining the different components of the YCW, concomitantly to the progression of the cells in the cycle would help solve this issue.

Several attempts have been published in the literature to stain the wall components. One recent publication<sup>59</sup> validates Trypan Blue as relevant stain for chitin, glucans and other molecules specific to plant cell walls, as its spectral properties are suited for confocal microscopy. However, performing these characterizations would require specific labelling of the cells and multiple washings of the sample that alter their proliferation, which are not compatible with an *in vivo* culture that preserves the yeast proliferation stages.

### 4.3 Statistical distributions of the mechanical parameters

We collect in Fig. 14 the  $\delta_{\alpha_m}$ ,  $\alpha_m$  and  $dF/d\delta_{\alpha_m}$  distributions computed from yeast cells compression in SMMLAC medium in the growth phase (exponential growth). To group the AFM series depending on the stage of proliferation, we analyzed the proliferation curves and their derivatives with standard theoretical growth models such as Verhulst, Gompertz or rational fractions<sup>27</sup>.

Interestingly, the occurrence of a maximum of  $\alpha_{eq}(\delta)$ , is observed independently of the stage of growth, however the mechanical parameters may change with the growth stage<sup>27</sup> (data not shown here). In the SMMLAC medium we observe in Fig. 14 that  $\delta_{\alpha_m}$  corresponding to the maximum values  $\alpha_m$  remains in the interval from 30 nm to 80 nm. We also observe that statistically, the greater  $\alpha_m$  values occur preferentially for larger  $\delta_{\alpha_m}$  and larger  $dF/d\delta_{\alpha_m}$ . If we consider that this increase of  $\alpha_{eq}$  during the first part of the compression experiment corresponds to the self-cancelling of one part of the YCW which reaches its compression limit, we could conclude that the stiffer cells with the largest effective tension could sustain greater compression forces. However, it is important to note that the range of  $\delta_{\alpha_m}$  values rarely extends beyond 100 nm, as if another deformation mechanism (the compression of the second sublayer for instance) would be systematically involved to release the mechanical stress and reverse the increase of the exponent  $\alpha_{eq}$ .

### 4.4 Experimental evidence for YCW multilayered structure

Clearly, in this study we confirm that the non-monotonous variation of  $\alpha_{eq}$  with  $\delta$  curves cannot be reproduced by spherical shell compression models; the composition, the fine structure of the wall can no longer be ignored. Yeast cell growth relies on an impressive mechanical wall machinery. These cells can support plastic deformations above a certain stress threshold, involving plastic components that would allow much larger deformations under stress<sup>60</sup>. More importantly, depending on their stage of growth, YCWs can become thinner and softer to facilitate their local stretch. Even if this softening is confined to a small fraction of the wall area, when these cells are compressed, these zones are likely to be prone to plastic deformation and failure. These phenomena have previously been reported<sup>4</sup>, and indeed by endowing their weaker and softer wall components with the ability to fluidise, yeast cells could become more resilient in critical environments.

Knowing the composition of the YCW and its multilayered structure is therefore essential for interpreting our measurements. The  $\beta$ -1,3 glucan-chitin complex is the major constituent of the

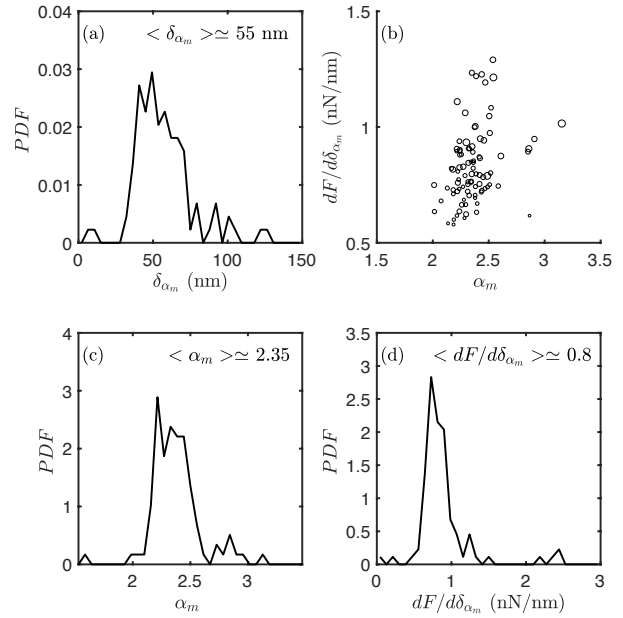


Fig. 14 Probability density functions computed from force curves compression of yeast cells in SMMLAC. (a) PDF of  $\delta_{\alpha_m}$ . (b) Scatter plot of  $dF/d\delta_{\alpha_m}$  versus  $\delta_{\alpha_m}$ . The size of the circles is proportional to  $\delta_m$ . (c) PDF of  $\alpha_m$ . (d) PDF of  $dF/d\delta_{\alpha_m}$ . 29 cells (giving a total  $29 \times 15 = 435$  force curves) have been selected from the growth phase to reconstruct these histograms.

inner wall. Chitin and  $\beta$ -1,6 glucans are minor components. Chitin is essentially a cross-linker of  $\beta$ -1,3 glucans and contributes to the insolubility of the fibres and  $\beta$ -1,6 glucans link the components of the inner and outer walls. On the outer surface of the wall we find mainly mannoproteins, which are extensively O- and N-glycosylated. Their dense packing limits the permeability of the wall to solutes. However, they are not as highly cross-linked as other glucan-based polymers of the wall and give the outer layer of the YCW greater plasticity or deformability. This outer layer of mannoproteins could play the role of a self-cancelling layer as proposed in our two-layer elastic model. In particular, changes that occur in the nanomechanical properties of the YCW, such as its tension, could be explained by the nature and complexity of the cross-linking network between  $\beta$ 1-6-glucans, mannans and chitin<sup>32,61–63</sup> and not simply by the percentage of each of these polymers.

Lactate, used in this study is a non-fermentable carbon source, and in this particular situation the hexose phosphates required for cell wall biosynthesis must be produced by the inverse process of glycolysis, gluconeogenesis, which is a more energetically demanding process. The growth rate is significantly reduced compared to other fermentable carbon sources, and moreover, with the lactate carbon source, less carbon source can be devoted to cell wall biosynthesis, resulting in a thinner YCW with a simpler architecture (less reinforcement by  $\beta$ -1,3-glucan cross-links in particular and  $\beta$ -glucan and chitin proportion dramatically reduced<sup>64</sup>). The comparison of the YCW tension evolution with proliferation stages will be examined in a forthcoming paper<sup>65</sup>.

#### 4.5 Taking modelling further: future developments

The two-component mechanical models that we have proposed here provided a quite satisfactory support for explaining which mechanism could produce the force curves that were recorded during compression of isolated yeast cells by a flat cantilever. One element that plays a key role in this respect is what we have called the ‘self-cancelling’ element, which describes a highly non-linear and sudden change close to a given distance ( $h$ ). Other mathematical forms could have been proposed, we do not argue that this formal model is mechanically relevant, but that it can reproduce in a mathematical sense what happens in the experiments. There is definitely a regime transition during compression that can be interpreted as a gradient in the composition and/or structure of the cell wall. We do not have the means to carry out further microscopic characterisation of YCWs, and we hope that our demonstration will stimulate further work.

A theoretical aspect that we have chosen not to discuss in detail here, because it would have required much more mathematical and technical development, concerns the possibility of modelling the cell wall as a mechanical component with continuously varying mechanical parameters, for example with  $R(\delta)$  or  $\alpha(\delta)$  forms. These functions are not simple constructions, since they challenge the foundations of convolution integrals, with mechanical kernels that would no longer be invariant with deformation (Volterra integrals). Since we limited our experiment to very small deformations, we believe that our hypothesis of kernel invariance is correct.

The advantage of the simple two-component models proposed here is that they can be straightforwardly implemented on computers to identify mechanical parameters such as  $R_i$ ,  $\ell_{i,0}$  to compare different yeast mutants through their mechanical response to compression. A generalisation of this two-layer elastic model to an  $n$ -layer model with  $n > 2$  can be done in the same line as Bonilla et al.<sup>23</sup>, as a first step towards a continuous model with a function  $\alpha(\delta)$ .

A complete mechanical model that takes into account the fine fibrillar structure of the wall should include a network of cross-linked elastic elements with a predefined geometry (random orientation, hierarchical, periodic organisation) for each sublayer, and the possibility of cross-linking between the different layers. Pieczywek and co-authors<sup>16</sup> give a brief review of the ongoing research on numerical models that have been constructed so far, and highlight important developments that could be made to include molecular ingredients for cell wall plasticity, elasticity, softening or loosening. Furthermore, the dynamic spatio-temporal organisation of the cell wall component during growth or its degradation remains a challenge for even the most sophisticated modelling techniques. Nevertheless, phenomenological models such as those proposed here can be constructed to approach the fascinating question of the real-time adaptation of a living walled unicellular organism to compressive strain.

#### Author contributions

L.D. performed the nano-indentation and yeast culture experiments, and designed the home-built batch reactor system, E.H. designed and guided the nano-indentation method, A.D. contributed expertise in yeast metabolism and biology and culture experiments and reviewed and edited the manuscript, P.A. contributed expertise in modelling and analysis and designed the analytical part of the multiscale model, reviewed and edited the manuscript, F.A. designed and managed the research project, designed the analytical methods and their implementation in a computer routine, analysed the experimental data, supervised the experiments and wrote the manuscript (original draft, review and editing). All authors have discussed and commented on the manuscript.

#### Conflicts of interest

There are no conflicts to declare

#### Acknowledgements

This work was supported by Agence Nationale de la Recherche (ANR) through contract: ANR-18-CE45-0012-01. L. Delmarre acknowledges the support of ANR for his PhD scholarship. L. Delmarre was appointed by University of Bordeaux from oct. 2022 to august 2023 as ATER (assistant professor). We are very thankful to A. Boudaoud for simulating remarks.

#### Notes and references

- 1 I. M. de Marañon, P.-A. Marechal and P. Gervais, *Biochemical and Biophysical Research Communications*, 1996, **227**, 519–523.
- 2 R. R. Lew, *Nature Reviews Microbiology*, 2011, **9**, 509–518.
- 3 P. Orlean, *Genetics*, 2012, **192**, 775–818.
- 4 R. Mishra, N. Minc and M. Peter, *Trends in Microbiology*, 2022, **30**, 495–510.
- 5 J. D. Stenson, P. Hartley, C. Wang and C. R. Thomas, *Biotechnology Progress*, 2011, **27**, 505–512.
- 6 S. Polizzi, B. Laperrousaz, F. J. Perez-Reche, F. E. Nicolini, V. M. Satta, A. Arneodo and F. Argoul, *New Journal of Physics*, 2018, **20**, 053057.
- 7 S. Polizzi, A. Arneodo, F.-J. Perez-Reche and F. Argoul, *Frontiers in Applied Mathematics and Statistics*, 2021, **6**, 613962.
- 8 S. Polizzi, F.-J. Perez-Reche, A. Arneodo and F. Argoul, *Physical Review E*, 2021, **104**, L052101.
- 9 B. P. Jena and J. H. Horber, *Atomic Force Microscopy in Cell Biology*, Academic Press - Elsevier, Amsterdam, L. Wilson, P. Matsudaira edn, 2002, vol. 68.
- 10 Y. Dufrene, *Life at the Nanoscale*, Pan Stanford Publishing Pte. Ltd., Singapore, 2011.
- 11 L. M. Rebelo, J. S. de Sousa, J. Mendes Filho and M. Radmacher, *Nanotechnology*, 2013, **24**, 055102.
- 12 I. Gammoudi, M. Mathelie-Guinlet, F. Morote, L. Beven, D. Moynet, C. Grauby-Heywang and T. Cohen-Bouhacina, *Colloids and Surfaces B: Biointerfaces*, 2016, **141**, 355–364.

- 13 S. B. Velegol and B. E. Logan, *Langmuir*, 2002, **18**, 5256–5262.
- 14 R. Mercade-Prieto, C. R. Thomas and Z. Zhang, *European Biophysics Journal*, 2013, **42**, 613–620.
- 15 S. Tsugawa, Y. Yamasaki, S. Horiguchi, T. Zhang, T. Muto, Y. Nakaso, K. Ito, R. Takebayashi, K. Okano, E. Akita, R. Yasukuni, T. Demura, T. Mimura, K. Kawaguchi and Y. Hosokawa, *Scientific Reports*, 2022, **12**, 13044.
- 16 P. M. Pieczywek, V. Chibrikov and A. Zdunek, *Biological Reviews*, 2023, **98**, 887–899.
- 17 S. Mani, D. J. Cosgrove and G. A. Voth, *The Journal of Physical Chemistry B*, 2020, **124**, 3527–3539.
- 18 V. V. Lulevich, D. Andrienko and O. I. Vinogradova, *The Journal of Chemical Physics*, 2004, **120**, 3822–3826.
- 19 L. Beauzamy, J. Derr and A. Boudaoud, *Biophysical Journal*, 2015, **108**, 2448–2456.
- 20 D. Vella, A. Ajdari, A. Vaziri and A. Boudaoud, *Physical Review Letters*, 2012, **109**, 144302.
- 21 D. Vella, A. Ajdari, A. Vaziri and A. Boudaoud, *Journal of The Royal Society Interface*, 2012, **9**, 448–455.
- 22 E. Couturier, D. Vella and A. Boudaoud, *The European Physical Journal E*, 2022, **45**, 13.
- 23 M. R. Bonilla, J. R. Stokes, M. J. Gidley and G. E. Yakubov, *Soft Matter*, 2015, **11**, 1281–1292.
- 24 G. Chagnon, M. Rebouah and D. Favier, *Journal of Elasticity*, 2015, **120**, 129–160.
- 25 F. Winston, C. Dollard and S. L. Ricupero-Hovasse, *Yeast*, 1995, **11**, 53–55.
- 26 C. L. Bouchez, N. Hammad, S. Cuvellier, S. Ransac, M. Rigoulet and A. Devin, *Frontiers in Oncology*, 2020, **10**, 1333.
- 27 L. Delmarre, *PhD thesis*, Universite Gustave Eiffel - Marne La Vallee (in French), 2023.
- 28 L. Delmarre, E. Harte, W. Bernabone and F. Argoul, *Journal of Visualized Experiments*, 2023, **preprint**, year.
- 29 S. Kasas and A. Ikai, *Biophysical Journal*, 1995, **68**, 1678–1680.
- 30 J. Arfsten, S. Leupold, C. Bradtmoller, I. Kampen and A. Kwade, *Colloids and Surfaces B: Biointerfaces*, 2010, **79**, 284–290.
- 31 J. M. Francois, C. Formosa, M. Schiavone, F. Pillet, H. Martin-Yken and E. Dague, *Current Genetics*, 2013, **59**, 187–196.
- 32 M. Schiavone, S. Dejean, N. Sieczkowski, M. Castex, E. Dague and J. M. Francois, *Frontiers in Microbiology*, 2017, **8**, 1806.
- 33 B. Caloca, A. Navarro, M. Canales-Torres, B. Le, C. Rosas, Z. Sero and J. Bachant, *Yeast*, 2022, **39**, 312–322.
- 34 JPK, *Nanowizard User Manuel*, 2012.
- 35 J. E. Sader, J. Lu and P. Mulvaney, *Review of Scientific Instruments*, 2014, **85**, 113702.
- 36 H.-J. Butt, B. Cappella and M. Kappl, *Surface Science Reports*, 2005, **59**, 1–152.
- 37 J. E. Sader, J. A. Sanelli, B. D. Adamson, J. P. Monty, X. Wei, S. A. Crawford, J. R. Friend, I. Marusic, P. Mulvaney and E. J. Bieske, *Review of Scientific Instruments*, 2012, **83**, 103705.
- 38 E. Harte, L. Delmarre and F. Argoul, *Technical report: Imaging micronsized objects under AFM cantilevers*, 2023.
- 39 M. Galluzzi, B. Zhang, H. Zhang, L. Wang, Y. Lin, X.-F. Yu, Z. Chu and J. Li, *Frontiers in Molecular Biosciences*, 2021, **8**, 669361.
- 40 M. R. Depaoli, H. Bischof, E. Eroglu, S. Burgstaller, J. Ramadani-Muja, T. Rauter, M. Schinagl, M. Waldeck-Weiermair, J. C. Hay, W. F. Graier and R. Malli, *Pharmacology & Therapeutics*, 2019, **202**, 98–119.
- 41 A. Grossmann and J. Morlet, *SIAM Journal on Mathematical Analysis*, 1984, **15**, 723–736.
- 42 S. Mallat and W. L. Hwang, *IEEE Transactions in Information Theory*, 1992, **38**, 617–643.
- 43 S. Digiuni, A. Berne-Dedieu, C. Martinez-Torres, J. Szecsi, M. Bendahmane, A. Arneodo and F. Argoul, *Biophysical Journal*, 2015, **108**, 2235–2248.
- 44 L. Streppa, F. Ratti, E. Goillot, A. Devin, L. Schaeffer, A. Arneodo and F. Argoul, *Scientific Reports*, 2018, **8**, 8602.
- 45 N. Gavara, *Scientific Reports*, 2016, **6**, 21267.
- 46 M. Radmacher, M. Fritz, C. Kacher, J. Cleveland and P. Hansma, *Biophysical Journal*, 1996, **70**, 556–567.
- 47 C. Correia-Melo, S. Kamrad, R. Tengolics, C. B. Messner, P. Trebulle, S. Townsend, S. Jayasree Varma, A. Freiwald, B. M. Heineike, K. Campbell, L. Herrera-Dominguez, S. Kaur Aulakh, L. Szyrwiel, J. S. Yu, A. Zeleznik, V. Demichev, M. Muller, B. Papp, M. T. Alam and M. Ralser, *Cell*, 2023, **186**, 63–79.e21.
- 48 R. Babazadeh, P.-J. Lahtvee, C. B. Adiels, M. Goksoy, J. B. Nielsen and S. Hohmann, *Scientific Reports*, 2017, **7**, 990.
- 49 W. Oliver and G. Pharr, *Journal of Materials Research*, 1992, **7**, 1564–1583.
- 50 L. Landau and E. Lifshitz, *Theory of Elasticity*, Pergamon Press, 3rd edn, 1986, vol. 7.
- 51 A. Pogorelov, *Translations of Mathematical Monographs*, 1988, **72**, 1–77.
- 52 B. Audoly and Y. Pomeau, *Elasticity and Geometry: From Hair Curls to the Non-linear Response of Shells*, Oxford University Press, Oxford ; New York, 2010.
- 53 E. Ventsel and T. Krauthammer, *Thin Plates and Shells: Theory, Analysis, and Applications*, Marcel Dekker, New York, 2001.
- 54 E. Gerasimova-Chechkina, L. Streppa, L. Schaeffer, A. Devin, P. Argoul, A. Arneodo and F. Argoul, *Journal of Rheology*, 2018, **62**, 1347–1362.
- 55 B. Laperrousaz, L. Berguiga, F. E. Nicolini, C. Martinez-Torres, A. Arneodo, V. M. Satta and F. Argoul, *Physical Biology*, 2016, **13**, 03LT01.
- 56 B. Laperrousaz, G. Drillon, L. Berguiga, F. Nicolini, B. Audit, V. M. Satta, A. Arneodo and F. Argoul, *AIP Conference Proceedings*, 2016, **1760**, 020040.
- 57 P. Milani, M. Gholamirad, J. Traas, A. Arneodo, A. Boudaoud, F. Argoul and O. Hamant, *The Plant Journal*, 2011, **67**, 1116–1123.
- 58 F. Cohen Tenoudji, *Analog and Digital Signal Analysis: From Basics to Applications*, Springer International Publishing,

- Cham, 2016.
- 59 J. Liesche, M. Marek and T. Główny-Pomorski, *Frontiers in Microbiology*, 2015, **6**, year.
- 60 J.-D. Julien and A. Boudaoud, *The Cell Surface*, 2018, **1**, 34–42.
- 61 E. Dague, R. Bitar, H. Ranchon, F. Durand, H. M. Yken and J. M. Francois, *Yeast*, 2010, **27**, 673–684.
- 62 R. A. Ribeiro, N. Bourbon-Melo and I. Sa-Correia, *Frontiers in Microbiology*, 2022, **13**, 953479.
- 63 R. A. Ribeiro, M. V. Vitorino, C. P. Godinho, N. Bourbon-Melo, T. T. Robalo, F. Fernandes, M. S. Rodrigues and I. Sa-Correia, *Scientific Reports*, 2021, **11**, 12652.
- 64 I. V. Ene, A. K. Adya, S. Wehmeier, A. C. Brand, D. M. MacCallum, N. A. R. Gow and A. J. P. Brown, *Cellular Microbiology*, 2012, **14**, 1319–1335.
- 65 L. Delmarre, E. Harte, A. Devin, P. Argoul and F. Argoul, *Elastic behavior of yeast cells with flat microlevers compression: Impact of growth stage and carbon source*, under review, 2023.